

H I-bearing dark galaxies predictions from constrained Local Group simulations: how many and where to find them

Guacimara García-Bethencourt¹, Arianna Di Cintio^{1,2}, Sébastien Comerón^{1,2}, Elena Arjona-Gálvez^{2,1}, Ana Contreras-Santos^{1,2}, Salvador Cardona-Barrero^{1,2}, Chris B. A. Brook^{1,2}, Andrea Negri^{1,4,5}, Noam I. Libeskind³ and Alexander Knebe^{1,6,7,8}

¹ Departamento de Astrofísica, Universidad de La Laguna, E-38200, La Laguna, Tenerife, Spain

² Instituto de Astrofísica de Canarias, Calle Via Láctea s/n, E-38206 La Laguna, Tenerife, Spain

³ Leibniz Institut für Astrophysik Potsdam (AIP), An der Sternwarte 16, D-14482, Potsdam, Germany

⁴ Facultad de Física, Universidad de Sevilla, Avda. Reina Mercedes s/n, Campus de Reina Mercedes, E-41012 Sevilla, Spain

⁵ INAF – Osservatorio di Astrofisica e Scienza dello Spazio di Bologna, Via Gobetti 93/3, I-40129 Bologna, Italy

⁶ Departamento de Física Teórica, Módulo 15, Facultad de Ciencias, Universidad Autónoma de Madrid, 28049 Madrid, Spain

⁷ Centro de Investigación Avanzada en Física Fundamental (CIAFF), Facultad de Ciencias, Universidad Autónoma de Madrid, 28049 Madrid, Spain

⁸ International Centre for Radio Astronomy Research, University of Western Australia, 35 Stirling Highway, Crawley, Western Australia 6009, Australia

Received XXX, XXXX; accepted XXX, XXXX

ABSTRACT

Context. *Dark galaxies* are small, dark-matter-dominated halos whose gas remains in hydrostatic and thermal equilibrium and has never formed stars. These systems are of particular interest because they represent a strong prediction of the Λ CDM model. As of today, only a handful of *dark galaxies* candidates have been observed so far, the most intriguing of which being Cloud-9.

Aims. Using several state-of-the-art hydrodynamical simulations, we aim to predict the abundance of *dark galaxies* expected within our Local Group, characterise their physical properties and provide guidance for their potential observational detection.

Methods. We analyse Local Group simulations with constrained initial conditions, each run with different codes, implementing different baryonic physics, feedback prescriptions, and employing two distinct values of star formation density threshold, $n_{\text{th}} = 0.13$ and 10 cm^{-3} , to select samples of dark and bright galaxies harboured in haloes of similar mass.

Results. We demonstrate that *dark galaxies* exist in all such simulations, though their number is larger in simulations that use a higher, more realistic n_{th} . These galaxies, whose gas remains diffuse and never forms stars, predominantly inhabit less-concentrated, higher-spin dark matter halos than their luminous counterparts. *Dark galaxies* are typically found in low-density regions at the outskirts of the Local Group, and their formation and evolution across redshift indicate that both the dark matter and gas densities in the surroundings of *dark galaxies* were consistently lower than those found around bright galaxies, making them less susceptible to interactions, mergers, or gas inflows. We estimate that up to 8 *dark galaxies* should be detectable in H I emission within 2.5 Mpc of the Local Group, with the FAST radio telescope, accounting for its sky coverage and minimum H I mass and column density.

Conclusions. Current hydrodynamical simulations of galaxies, combined with upcoming H I surveys, will offer a direct and powerful test of Λ CDM through their ability to predict and measure properties of *dark galaxies* within and beyond the Local Group.

Key words. Methods: numerical – Galaxies: formation – Galaxies: evolution – Galaxies: Local Group – Galaxies: dwarf – Cosmology: dark matter

1. Introduction

Within the Λ CDM model, galaxies form hierarchically through the gravitational collapse of small dark matter (DM) structures (White & Rees 1978), which then merge to form larger systems. This progressive growth of structures builds the DM halos in which galaxies are embedded, enabling them to accrete gas that later cools and create stars. In this framework of cold DM bottom-up assembly of structures, we expect a large number of low-mass DM halos. Some of these halos may have low stellar mass content or even be starless. These objects are called *dark galaxies*, due to their expected DM dominated nature (e.g. Trentham et al. 2001; Kent et al. 2007).

As being such a strong prediction of the Λ CDM model, finding *dark galaxies* has been one of the main objectives of world-class radio telescopes such as the Arecibo radio telescope,

through its Arecibo Legacy Fast ALFA (ALFALFA) Survey (Giovanelli et al. 2005; Haynes et al. 2011), and the more recent Five-Hundred-Meter Aperture Spherical Telescope (FAST; Zhang et al. 2024).

Theoretically, it has been demonstrated that only structures with masses above a certain redshift-dependent critical mass are able to retain gas in their potential well to form stars and become luminous galaxies (e.g. Hoeft et al. 2006; Okamoto et al. 2008; Benítez-Llambay & Frenk 2020). This critical mass is $M_{\text{crit}} \approx 5 \times 10^9 M_{\odot}$ at the present day (Benítez-Llambay & Frenk 2020; Nebrin et al. 2023), and it depends on the time at which reionisation took place and on the mass assembly rate of each galaxy. Thus, reionisation plays an essential role in the galaxy evolution process, as it can quench and avoid star formation (SF) in small halos, by photoheating and removing their gas (e.g. Benítez-Llambay et al. 2017). Those small halos that

are able to retain cold and dense gas to form neutral hydrogen (HI) at their centres, but are affected by cosmic reionisation in such manner (i.e. have currently zero or few stars) have been dubbed REionisation-Limited HI Clouds or RELHICs (Benítez-Llambay et al. 2017). These cover a halo mass range between $\sim 10^8 M_\odot$ and $\sim 5 \times 10^9 M_\odot$, and are equivalent to the mini-halos initially proposed by Rees (1986) and Ikeuchi (1986).

Due to their nature, RELHICs/*dark galaxies* are challenging to observe. In fact, there are no confirmed *dark galaxies*, but there are a few candidates like Cloud-9 (Zhou et al. 2023; Benítez-Llambay & Navarro 2023), or more recently, Candidate Dark Galaxy-2 or CDG-2 (Li et al. 2025b), among others. As for Cloud-9, these objects can potentially be detected as sources of HI 21 cm emission without an apparent stellar counterpart, using instruments like FAST.

Cloud-9 is a potential starless *dark galaxy*, detected as an HI cloud close to M94, and appears to be devoid of a stellar component within the DESI Imaging Legacy Survey (DESI LS) surface brightness limit (Martínez-Delgado et al. 2023). It is a gas-rich object with $M_{\text{H}\text{I}} \approx 10^6 M_\odot$ (Benítez-Llambay et al. 2024) and DM halo mass of $M_{200} \sim 5 \times 10^9 M_\odot$ (Zhou et al. 2023; Benítez-Llambay & Navarro 2023). Following the predictions by Benítez-Llambay et al. (2017), it presents a gas temperature of $T \sim 2 \times 10^4$ K. Cloud-9 is estimated to be located at a distance of $d \sim 4.7$ Mpc (upper limit of ~ 10 Mpc) and have a halo concentration of $c_{\text{NFW}} \sim 13$ (Benítez-Llambay & Navarro 2023).

CDG-2 is also a recent prospective candidate for Ultra-Diffuse/*dark galaxy*, first identified by Li et al. (2025a) through the faint and diffuse emission of its population of globular clusters with the *Hubble Space Telescope* (*HST*). It is located in the Perseus cluster, at a distance of 75 Mpc, and has a total stellar mass of $M_* \approx 1.2 \times 10^7 M_\odot$, and a halo mass of $M_{\text{halo}} \approx 2 - 5.7 \times 10^{10} M_\odot$, which indicates that it resides in a massive DM halo (Li et al. 2025b).

In this context, numerical simulations developed within ΛCDM are an important tool that can help us test results and make predictions on the nature of *dark galaxies*. In particular, simulations of the Local Group are key to understand the main drivers for the formation and evolution of the galaxies residing within, as well as their environmental dependence.

For example, in the work by Benítez-Llambay et al. (2017), they analysed the properties of RELHICs in a Local Group environment with the APOSTLE cosmological zoom-in simulations (Fattahi et al. 2016; Sawala et al. 2016). Their results showed that these systems harbour gas and reside beyond 500 kpc from the Milky Way (MW), with most of their gas in an ionized state, except for a small nearly spherical HI core. Moreover, the gas in these systems was found to be in hydrostatic equilibrium with the underlying NFW halo (Navarro-Frenk-White; Navarro et al. 1996, 1997) and in thermal equilibrium with the cosmic UV radiation background. However, the original APOSTLE simulations of the Local Group were affected by an overproduction of stars at a fixed halo mass (Sawala et al. 2016), which casts doubts about the predicted number of *dark galaxies* found within them.

More recently, Lee et al. (2024) use simulations from the IllustrisTNG project (e.g. Nelson et al. 2019; Pillepich et al. 2019) to explore the nature of *dark galaxies*. Within the TNG50 volume, they identify *dark galaxies* with DM halo masses $\sim 10^9 h^{-1} M_\odot$ and stellar-to-total mass ratios $M_*/M_{\text{tot}} < 10^{-4}$ at $z = 0$. They find that *dark galaxies* live mainly in voids and tend to be larger in size and have larger spin parameters than their luminous counterparts (see also Jimenez & Heavens 2020). However, the TNG50 simulation shares a similar issue of overcooling as the APOSTLE simulations. More specifically,

below a halo mass of $10^{11} M_\odot$, most dwarf galaxies tend to overproduce the number of stars compared to the expected abundance matching relations (Moster et al. 2013; Brook et al. 2014; Girelli et al. 2020). On top of this, Lee et al. (2024) do not require their *dark galaxies* sample to explicitly contain gas, making thus difficult to use their predictions in light of upcoming HI surveys. The tendency of *dark galaxies* to live in low density regions has also been recently explored observationally in Kwon et al. (2025), who study the properties of a selection of prospective *dark galaxy* candidates from the ALFALFA Survey (Haynes et al. 2018).

In this work, we move forward by studying the number, distribution and characteristics of *dark galaxies* arising in different sets of zoom-in Local Group simulations, and offer concrete predictions on their detectability with radio telescopes. For this analysis, we identify *dark galaxies* in four simulated Local Group runs employing constrained initial conditions: three from the HESTIA simulations (Libeskind et al. 2020) and one from the new NIVARIA-LG simulation (Contreras-Santos et al. in prep.). In particular, the three high-resolution HESTIA runs reach down to $1.5 \times 10^5 M_\odot$ in DM particle mass and 220 pc in spatial resolution. In contrast, the TNG50 simulations have a DM particle mass resolution of $4.5 \times 10^5 M_\odot$ and a softening length of 330 pc. The NIVARIA-LG simulations, on the other side, although lower in resolution than HESTIA, closely follow the expected abundance matching relation at all masses, lending confidence to the reliability of their *dark galaxy* predictions.

We explore the properties of *dark galaxies* within these simulations which are run with different codes, galaxy formation models, baryonic physics, feedback implementations, resolutions, and SF density thresholds, with the aim of validating whether *dark galaxies* can be found across different simulation setups. Our goal is to characterize the main properties of HI -bearing *dark galaxies* in Local Group-like environments and to study their evolution over time, shedding light on their nature and uncovering details of their origin and formation pathways. To better understand these objects, we compare our *dark galaxy* sample with a sample of bright galaxies, i.e. luminous galaxies within the same halo mass range. Additionally, we treat Cloud-9 as a reference for our simulated *dark galaxies* and test our results against the HI detection limits of the FAST radio telescope.

We describe the simulation sets in detail in Section 2. In Section 3, we present the selection criteria and resulting samples of dark and bright galaxies from each simulation, including properties of the underlying DM halos, gas content, environmental effects, and HI detectability with FAST. Section 4 provides a discussion of the results, and Section 5 summarizes the main conclusions.

2. Simulations

We employ two different sets of cosmological hydrodynamical simulations that reproduce the properties of the Local Group, including two massive central haloes that are analogues of the MW and M31. These simulation suites consist of the three high-resolution simulations from the HESTIA project (Libeskind et al. 2020) and a lower-resolution simulation named NIVARIA-LG (Contreras-Santos et al. in prep.). Both sets are zoom-in simulations run from an original cosmological box of size $100 h^{-1}$ Mpc. The simulations adopt the parameters of a ΛCDM Planck cosmology (Planck Collaboration et al. 2014), i.e. $\Omega_m = 0.307$, $\Omega_b = 0.048$, $\Omega_\Lambda = 0.693$, $\sigma_8 = 0.8288$, and $H_0 = 100 h \text{ km s}^{-1} \text{ Mpc}^{-1}$, where $h = 0.6777$. They also

employ constrained initial conditions derived from observations of the peculiar velocity field in the CosmicFlows-2 catalogue (Tully et al. 2013), which are constructed to replicate the main large-scale structures of the Local Volume at $z = 0$ (e.g. a Local Group-like pair, a Virgo Cluster-like halo; Hoffman & Ribak 1991; Zaroubi et al. 1999). For both suites, the properties of the haloes are derived using the Amiga Halo Finder¹ (AHF; Gill et al. 2004; Knollmann & Knebe 2009), which defines haloes as over-densities of DM with $\Delta \sim 200$ times the critical density of the Universe at $z = 0$, $\rho_c = 3H_0^2/(8\pi G)$. AHF is also used to trace haloes across snapshots, i.e. to construct a merger tree that connects haloes between consecutive time steps in the simulations. For the analysis and post-processing of the simulations, we make use of the PYNBODY² package (Pontzen et al. 2013).

Despite the parallels between the two sets of simulations, they were run with different codes, subgrid physics, feedback prescriptions, and SF models. These differences make the HESTIA and NIVARIA-LG simulations ideal for comparison and for assessing the robustness of our results. A more detailed description of the simulations used is provided below.

2.1. HESTIA simulations

We use the three highest-resolution simulations from the ‘High-resolutions Environmental Simulations of The Immediate Area’ HESTIA project, whose initial conditions seeds are named 09_18, 17_11 and 37_11 (Libeskind et al. 2020). HESTIA is the successor of the original ‘Constrained Local UniversE Simulations’ CLUES project³ (Gottloeber et al. 2010; Libeskind et al. 2010; Carlesi et al. 2016; Sorce et al. 2016). The high-resolution region consists in two spheres of 3.7 Mpc ($2.5 h^{-1} \text{ Mpc}$) of radius centred on the two main halos of each run at $z = 0$. The particle masses resolution for DM and gas are $m_{\text{DM}} = 1.5 \times 10^5 M_{\odot}$ and $m_{\text{gas}} = 2.2 \times 10^4 M_{\odot}$, respectively. The softening length is $\epsilon = 220 \text{ pc}$. These simulations were run with the AURIGA galaxy formation model (Grand et al. 2017) employing the AREPO N-body moving-mesh code (Springel 2010; Pakmor et al. 2016; Weinberger et al. 2020). The formation model incorporates magnetic fields and super-massive black holes (SMBHs) physics. A spatially uniform UV background is set as an ionising source of radiation, which completes the reionisation epoch at $z \sim 6$ (Vogelsberger et al. 2013). Gas cooling is implemented for primordial gas and metals (Vogelsberger et al. 2013). Gas is converted into stars stochastically following a Kennicutt–Schmidt relation (Schmidt 1959; Kennicutt 1998) when its density reaches values larger than $n_{\text{th}} = 0.13 \text{ cm}^{-3}$. Gas that satisfies this density criterion follows a two-phase subgrid model that distinguishes between cold and hot components of the interstellar medium (ISM; Springel & Hernquist 2003). An effective equation of state is applied to maintain pressure equilibrium in the star-forming gas (e.g. Grand et al. 2017).

2.2. NIVARIA-LG simulations

The ‘Numerical InVESTigation of dwARF galaxies Including AGN feedback in the Local Group’, NIVARIA-LG project (Contreras-Santos et al. in prep.), is a new set of simulations whose initial conditions are drawn from one of the HESTIA intermediate-resolution runs, and are based on the galaxy formation model from the NIHAO (Wang et al. 2015) and MaGICC

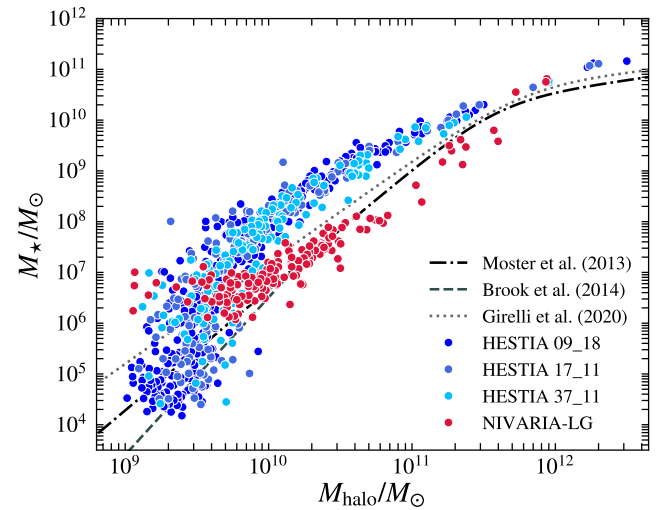


Fig. 1. M_{\star} – M_{halo} relation for isolated halos within our simulated Local Groups, containing gas and stars and with DM halo masses between $10^9 M_{\odot}$ and $10^{12.5} M_{\odot}$. Halos from the HESTIA simulations are coloured in shades of blue and halos from NIVARIA-LG in red. The M_{\star} – M_{halo} relations from Moster et al. (2013), Brook et al. (2014), and Girelli et al. (2020) are shown in dashed and dotted lines.

(Stinson et al. 2012; Brook et al. 2012) projects, which have been shown to follow well observed galaxy scaling relations (e.g. Brook et al. 2012; Wang et al. 2015; Macciò et al. 2016; Dutton et al. 2017; Santos-Santos et al. 2018).

The simulations comprise two analogue runs: one in which a SMBH is seeded at the centre of haloes exceeding $M_{\text{halo}} \sim 10^{10} M_{\odot}$, and another in which SMBH seeding is disabled. In this work, we use the run without the SMBH implementation. The cosmological initial conditions used to generate the Local Group environment in NIVARIA-LG are drawn from one of the HESTIA intermediate-resolution runs, following an approach similar to that adopted in Arora et al. 2022. The zoom-in region of NIVARIA-LG consists of a sphere of radius $5h^{-1} \text{ Mpc}$ centred on the Local Group. The particle masses for DM and gas are $m_{\text{DM}} = 1.6 \times 10^6 M_{\odot}$ and $m_{\text{gas}} = 3 \times 10^5 M_{\odot}$, respectively. The minimum gravitational softening lengths are $\epsilon_{\text{DM}} = 860 \text{ pc}$ for DM and $\epsilon_{\text{gas}} = 488 \text{ pc}$ for gas. This cosmological hydrodynamical simulation is run with a modified version of the Smoothed Particle Hydrodynamics (SPH) code GASOLINE2 (Wadsley et al. 2017), similar to that used in Blank et al. (2019). Gas and metal-line cooling are implemented for H, He, and several metal species (Shen et al. 2010), using CLOUDY (Ferland et al. 1998). A uniform UV background (Haardt & Madau 1996) provides ionising radiation and heating of the medium, modelling reionisation, which completes at $z \sim 6$. The density threshold for SF is set to $n_{\text{th}} = 10 \text{ cm}^{-3}$, consistent with the densities of giant molecular clouds. Gas is also required to have a temperature below $T_{\text{th}} = 1.5 \times 10^4 \text{ K}$. Star formation follows a Chabrier (2003) IMF and the Kennicutt–Schmidt relation (Schmidt 1959; Kennicutt 1998). Supernovae types Ia and II, as well as early stellar feedback (Stinson et al. 2012), are included to inject energy and metals into the surrounding medium in both runs.

An important difference arising from the distinct subgrid models and feedback implementations in the two simulation suites is that HESTIA tends to form more stars than expected from observations at fixed halo mass. As a result, HESTIA galaxies lie systematically above the empirical stellar-to-halo mass

¹ <http://popia.ft.uam.es/AHF/>

² <https://pynbody.readthedocs.io/latest/>

³ www.clues-project.org

Table 1. Sample of halos resulting from the selection described in section 3.1 for each simulation. The first column lists the label assigned to each simulation. The second column provides the total mass contained within 2.5 Mpc of the corresponding MW analogue. The third column reports the total number of halos identified within 2.5 Mpc of the MW and with halo masses between 10^9 and $10^{10} M_\odot$ using the selection criteria. The fourth column shows the number of bright galaxies, while the fifth column lists the number of *dark galaxies* in each simulation. The final column displays the number of *dark galaxies* from the previous column that are completely starless. Values in brackets indicate halos that are satellites of other galaxies (i.e. systems that are not isolated).

Sim.	M_{tot} ($10^{12} M_\odot$)	n_{total}	n_{bright}	n_{dark}	n_{starless}
HESTIA 09_18	13.03	187 (27)	84 (18)	32 (0)	17
HESTIA 17_11	10.77	139 (14)	56 (11)	22 (0)	11
HESTIA 37_11	7.67	133 (25)	53 (19)	1 (1)	0
NIVARIA-LG	5.51	81 (9)	15 (4)	59 (5)	59

($M_\star - M_{\text{halo}}$) relation, as seen in Fig. 1. This overproduction of stars, associated with the Springel & Hernquist (2003) model, has been noted previously (e.g. Benítez-Llambay et al. 2013; Arjona-Gálvez et al. 2025), and is particularly pronounced for haloes with masses between $10^{10} M_\odot$ and $10^{11} M_\odot$. Conversely, owing to their different SF criteria and feedback prescriptions, NIVARIA-LG haloes follow the empirical relations more closely. This contrast allows us to bracket the expected number of *dark galaxies* providing upper and lower limits from the two simulation suites as a reference for observational expectations.

3. Results

3.1. Dark galaxy selection sample

We select samples of *dark galaxies* and bright galaxies from each simulation at $z = 0$. Both samples are defined within a sphere of 2.5 Mpc in radius centred on the MW analogues in order to ensure the search within the highest-resolution regions of the Local Group. We select only those halos with a DM halo mass in the $[10^9 - 10^{10}] M_\odot$ range and a fraction of high-resolution DM particles larger than 0.98.

Here, we define *dark galaxies* as those halos that, following the conditions described above, have ≤ 10 stellar particles, and ≥ 10 gas particles. This is $\lesssim 10^5 M_\odot$ in stellar mass, and $\gtrsim 10^5 - 10^6 M_\odot$ in gas mass, depending on the resolution of the simulations. The number of gas particles was chosen to guarantee that the predicted *dark galaxies* preserve sufficient gas to remain detectable with radio telescopes. On the other hand, we select a sample of bright galaxies as those halos containing more than 10 stellar particles. In this case, we do not restrict to a minimum number of gas particles. Hence, some of these halos could be gas-free at $z = 0$ (and hence non-star forming), due to gas exhaustion after SF, ram pressure stripping (Gunn & Gott 1972) or other processes such as interaction with the cosmic web (e.g. Benítez-Llambay et al. 2013).

Table 1 shows the number of haloes found after applying the selection cuts described above. From the second and third columns, we note that, as expected, the total number of galaxies depends on the total mass of the simulation within our designated region, with the most massive simulation containing the largest number of haloes. However, the number of bright galaxies in the HESTIA simulations is much larger than the number of *dark galaxies*, whereas the opposite is true for NIVARIA-LG. This difference is likely a consequence of the different SF den-

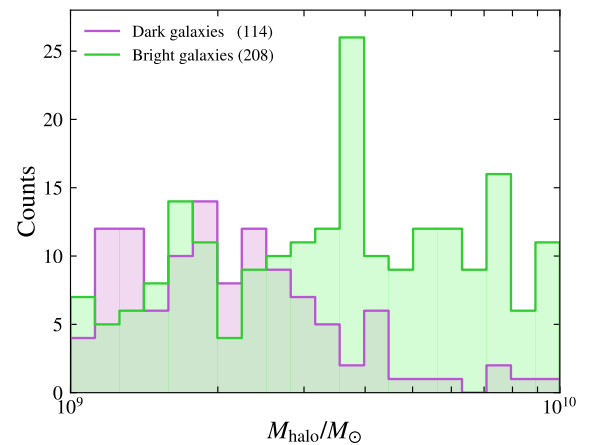


Fig. 2. Number of halos from the four simulations as a function of the DM halo mass. The total sample of *dark galaxies* is shown in magenta and the total sample of bright galaxies is shown in green.

sity thresholds employed in the two simulation sets. Therefore, we do not apply any mass rescaling to the predicted numbers of dark and bright galaxies based on the total Local Group mass, as these numbers depend not only on mass but also on the underlying subgrid physics models of each simulation. Finally, the number of satellites in each sample is indicated in brackets, i.e., haloes belonging to a central or host galaxy. In both HESTIA and NIVARIA-LG, a much higher fraction of bright galaxies are satellites compared to *dark galaxies*, suggesting that bright galaxies tend to reside closer to other systems and may experience more interactions.

It is important to note that the selection cuts for *dark galaxies* could be affected by the different particle resolutions of HESTIA and NIVARIA-LG. In the case of the stellar particle cut, the lower resolution of NIVARIA-LG does not impact the *dark galaxy* sample, since all these haloes are completely starless at $z = 0$.

To visualize the distribution of the sample, Fig. 2 shows the number of dark and bright haloes as a function of DM halo mass, combining all the simulation sets. The values in brackets in the legend correspond to the total number of halos for each case. Bright galaxies dominate the more massive halo region of the plot, whereas *dark galaxies* are more abundant in the lower-mass end of the distribution. This tendency is consistent with the galaxy sample selection from Lee et al. (2024).

In the top panel of Fig. 3, we show the $M_\star - M_{\text{halo}}$ relation for dark and bright galaxies at $z = 0$ (referred as DGs and BGs in legends hereafter, respectively), in tandem with the semi-empirical relations from Moster et al. (2013), Brook et al. (2014), and Girelli et al. (2020). Similarly, we show the relation between the gas and the halo masses in the central panel, and the relation between H_1 gas and halo masses at the bottom (see Sec. 3.5 for details on how H_1 is computed in each simulation). Cloud-9 is included in the top and bottom panels for reference, assuming $M_{200} \sim 5 \times 10^9 M_\odot$ (Benítez-Llambay & Navarro 2023), an upper stellar mass limit of $10^5 M_\odot$ (Zhou et al. 2023; Benítez-Llambay et al. 2024), and $M_{\text{H}_1} \approx 10^6 M_\odot$ (Benítez-Llambay et al. 2024). It falls within the massive end of our *dark galaxies* region.

In the top panel of the figure, we see a clear separation between dark and bright galaxies in the y-axis, around $10^5 M_\odot$ in stellar mass and a large number of starless halos, especially for NIVARIA-LG, which we show as squares. More specifically, the

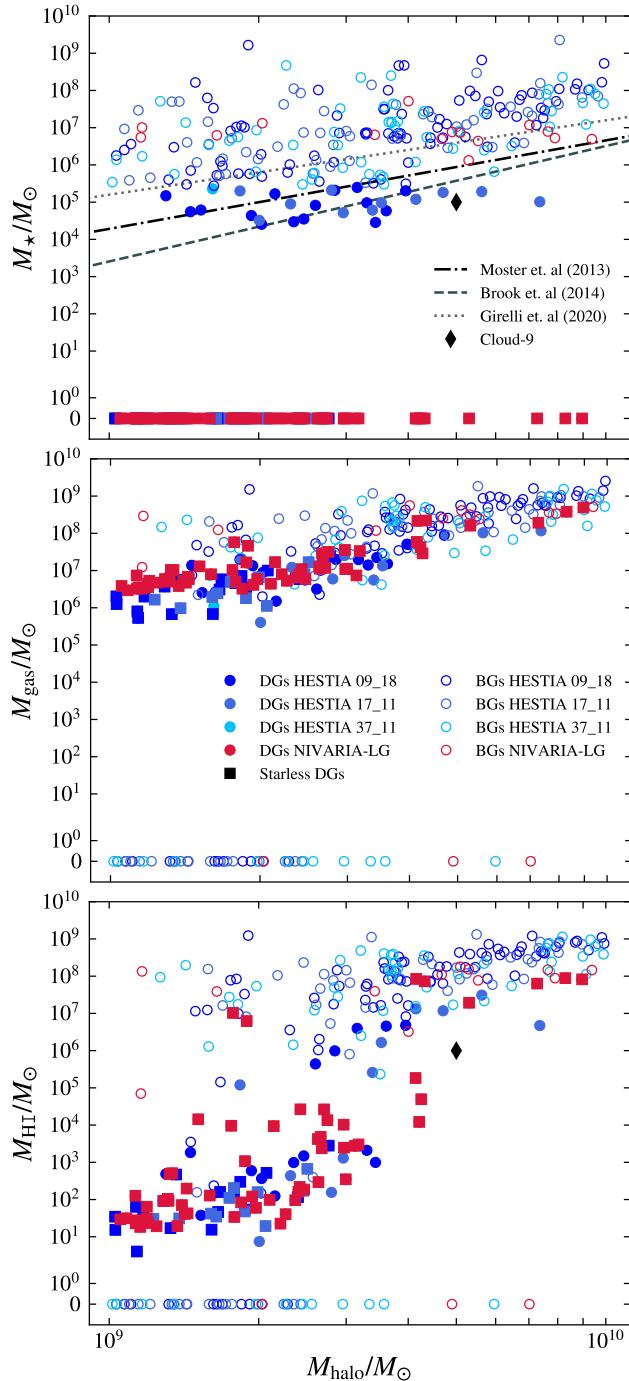


Fig. 3. M_\star - M_{halo} relation (top), gas-to-halo mass relation (centre), and H_1 -to-halo mass relation (bottom), for dark (filled markers) and bright (empty markers) galaxies at $z = 0$. Halos from the HESTIA simulations are coloured in shades of blue and halos from NIVARIA-LG are in red. Circles indicate *dark galaxies* with stars, whereas squares indicate starless *dark galaxies*. In the top panel, the M_\star - M_{halo} relations from Moster et al. (2013), Brook et al. (2014), and Girelli et al. (2020) are shown in dotted-dashed, dashed, and dotted lines, respectively. We include Cloud-9 as a black diamond in the top and bottom panels.

number of starless *dark galaxies* in our sample is 17 for the HESTIA 09_18 run, 11 for HESTIA 17_11, 0 for HESTIA 37_11, and 59 for the NIVARIA-LG simulation (see Table 1). That is, the whole sample of NIVARIA-LG *dark galaxies* is composed of completely starless objects.

On the other hand, in the central panel, the total gas mass exhibits a clear correlation with DM halo mass, and the dark and bright galaxy samples appear broadly similar in this respect. Some bright galaxies, however, have no gas content and are therefore non-star-forming at the present time. In contrast, in the bottom panel of Fig. 3, the H_1 gas content differs between the two samples: only the most massive *dark galaxies* have H_1 masses comparable to their bright counterparts, i.e., $M_{H_1} > 10^5 M_\odot$ for $M_{\text{halo}} > 10^{9.5} M_\odot$.

3.2. Dark matter halos properties

In this section, we tackle the evolution of DM halo mass and its relation to reionisation, as well as intrinsic properties of the halos, like the concentration and the spin parameter.

In order to analyse the impact of reionisation, we need to estimate the evolution with time of the minimum critical halo mass needed for gas to collapse and form stars. Following the scheme given in Benítez-Llambay & Frenk (2020), before reionisation the critical DM halo mass corresponds to the one above which atomic hydrogen can cool efficiently to form stars:

$$M_{\text{H}}^z \sim (4 \times 10^7 M_\odot) \left(\frac{1+z}{11} \right)^{-3/2}, \quad (1)$$

On the other hand, after reionisation sets off, the critical DM halo mass for which gas can collapse within halos is:

$$M_{\text{crit}}^z \sim (10^{10} M_\odot) \left(\frac{T_b}{3.2 \times 10^4 \text{ K}} \right)^{3/2} (1+z)^{-3/2}, \quad (2)$$

where T_b refers to the virial temperature of the halo.

In Fig. 4, we show such critical mass as a function of z . We compare the median halo mass evolution of our dark (dotted-dashed lines) and bright (solid lines) galaxies for HESTIA simulations in blue and NIVARIA-LG in red, together with theoretical predictions. Here, the cyan dashed line represents M_{crit}^z for a fixed halo with $T_b = 2 \times 10^4$ and the orange line represents M_{H}^z . By combining the two relations prior and after reionisation, Benítez-Llambay & Frenk (2020) show the global critical mass for which gas can collapse across redshift, represented in Fig. 4 by the black dotted-dashed line, leading to a minimum halo of $M_{200} \sim 5 \times 10^9 M_\odot$ at $z = 0$. Thus, a halo that lies below the black dotted-dashed line should remain completely dark (see also Pereira-Wilson et al. 2023). This plot displays a substantial difference between dark and bright galaxies, where the former tend to lie close or below the critical mass, whilst the latter are well above the black line at all z , indicating their luminous nature.

We can observe that *dark galaxies* generally form later-on than bright galaxies, being their half-mass accretion time $z_{\text{dark}} = 2.0$ and $z_{\text{dark}} = 1.7$ for NIVARIA-LG and HESTIA, respectively, while the formation time of the corresponding bright galaxies is between $z_{\text{bright}} = 3.2$ and $z_{\text{bright}} = 2.6$. This result is in agreement with findings presented in Lee et al. (2024) (their Fig. 5 and discussion therein). In Fig. 4 it is also clear that bright galaxies, which are overall more massive than *dark galaxies* (see Fig. 2), were already more massive prior to reionisation, making them less vulnerable to the effects of a ionizing background. The later formation times of *dark galaxies* should be reflected in the concentration parameters of their dark-matter halos, as these systems formed in a less dense Universe.

Figure 5 shows the relation between the halo mass and the concentration corresponding to DM halos with a NFW profile at

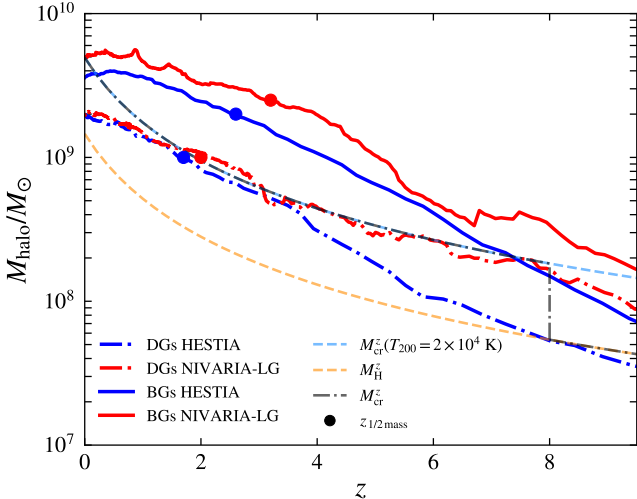


Fig. 4. Evolution of the median DM halo masses of *dark galaxies* (dotted-dashed lines) and *bright galaxies* (solid lines) as a function of redshift. Red lines represent the median of all halos of the NIVARIA-LG simulation, whilst blue lines correspond to the median of all halos for the HESTIA runs. The red and blue dots indicate the redshifts at which the galaxies reach half of their final halo mass. Following the scheme from Benitez-Llambay & Frenk (2020), we show by the black dotted-dashed line the critical mass needed for gas to collapse. In addition, the cyan dashed line shows the critical halo mass for a fixed virial temperature of $T_b = 2 \times 10^4$ K. The orange dashed line represents the halo mass above which atomic hydrogen cooling is efficient.

$z = 0$, where the black dashed line represents the c_{200} - M relation from Dutton & Macciò 2014, following a Planck cosmology.

In this figure, the grey dotted-dashed line corresponds to the lineal fit of the data (both dark and bright galaxies), and the shaded region is the 3σ scatter between this fit and the Dutton & Macciò (2014) relation. As expected, we see that the *dark galaxy* sample has less concentrated DM halos than bright galaxies at a fixed halo mass. Quantitatively, *dark galaxies* have a median value of $c_{\text{NFW, dark}} = 11.1 \pm 0.5$, and bright galaxies a median value of $c_{\text{NFW, bright}} = 18.6 \pm 0.5$. Cloud-9, also added in the plot, lies close to the Dutton & Macciò (2014) relation.

We then study the spin parameter of the DM halos in both samples, shown in Fig. 6. The spin parameter, λ , is defined by the following expression (Bullock et al. 2001):

$$\lambda = \frac{|\mathbf{J}|}{\sqrt{2}MRV}, \quad (3)$$

where \mathbf{J} is the angular momentum of a sphere with mass M and radius R , and V is the circular velocity at R .

We compare with the log-normal distribution from Bullock et al. (2001) as a reference. *Dark galaxies* (coloured in magenta) show larger spin parameters than bright galaxies (coloured in green), with median values of $\lambda_{\text{dark}} = 0.036 \pm 0.003$ and $\lambda_{\text{bright}} = 0.026 \pm 0.002$, respectively. The significance in the difference between both distributions is confirmed by applying the Kolmogorov-Smirnov (KS) test, which results in a p -value of $\sim 10^{-5}$. The larger spin parameters of *dark galaxies* are directly related to their lower concentrations and may hinder the retention and condensation of gas to form stars, leading to lower gas densities as well (see also Jimenez & Heavens 2020 and Lee et al. 2024).

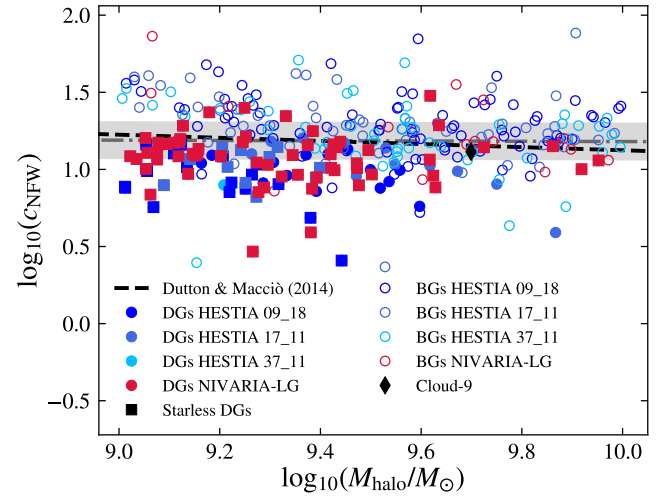


Fig. 5. Concentration-halo mass relation for dark (filled markers) and bright (empty markers) galaxies at $z = 0$, colour-coded as in Fig. 3. The black dashed line is the c_{200} relation drawn from Dutton & Macciò (2014), and the grey line represents a lineal fit of both the dark and bright sample together, i.e. $\log_{10}(c_{\text{NFW}}) = -0.01 \log_{10}(M_h/M_\odot) + 1.27$. The shaded region shows the 3σ scatter of both relations.

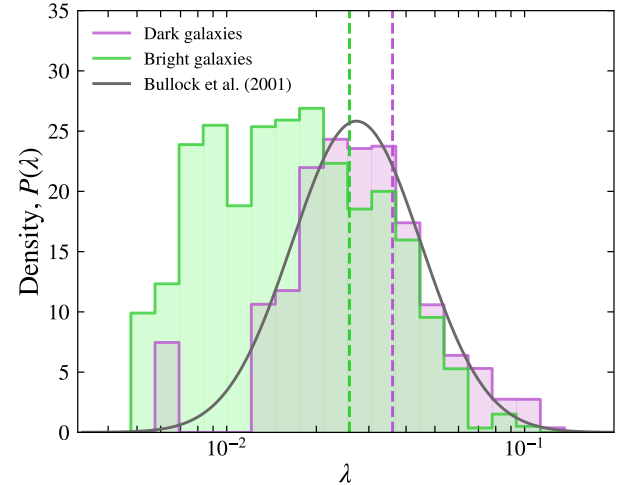


Fig. 6. Probability density distribution of the spin parameter of the DM halo, $P(\lambda)$, for *dark galaxies* in magenta and *bright galaxies* in green in all four simulations. The vertical dashed lines indicate the median values for each distribution, being $\lambda_{\text{dark}} = 0.036 \pm 0.003$ for *dark galaxies*, and $\lambda_{\text{bright}} = 0.026 \pm 0.002$ for *bright galaxies*. The solid grey line represents the log-normal fiducial distribution from Bullock et al. (2001).

3.3. Gas content and thermodynamic properties

We study the temperature and density of the gas in both dark and bright galaxies. The relation between these two properties at $z=0$ is shown in Fig. 7 as a 2D histogram of gas particles aggregated over all galaxies in each sample. The top row corresponds to *dark galaxies*, while the bottom row shows bright galaxies. Each column corresponds to a different simulation, from left to right HESTIA 09_18, 17_11, 37_11, and NIVARIA-LG. Regardless of the particular simulation, *dark galaxies* do not exhibit the characteristic star-forming regions in the T - ρ phase diagram, as they lack gas at densities above the threshold required for SF, indicated by the vertical cyan and white line, for HESTIA and

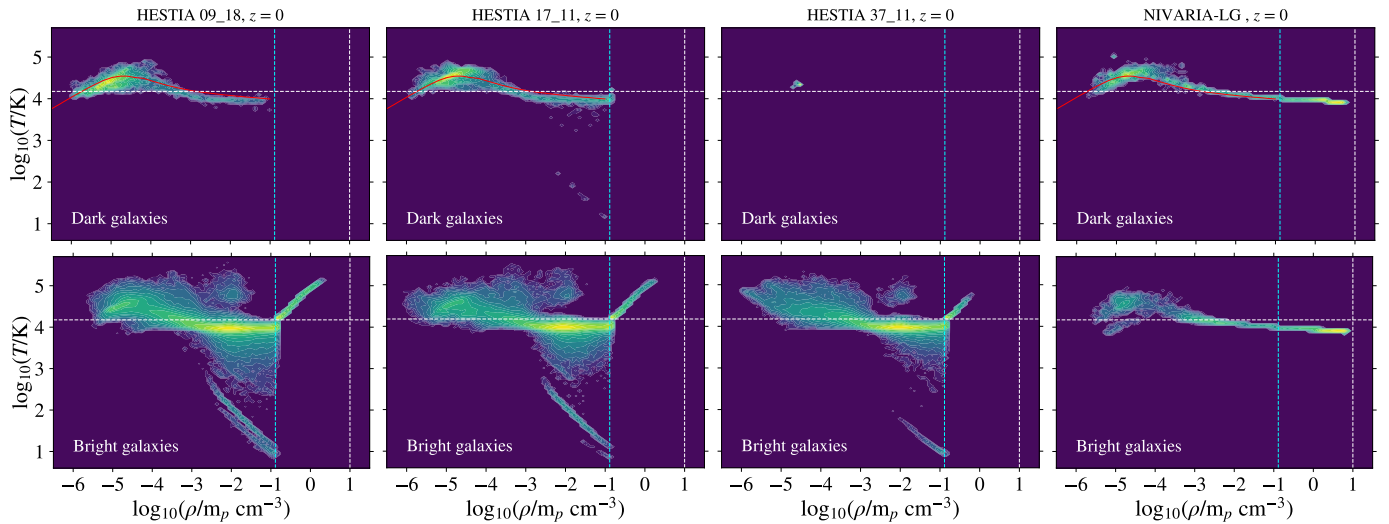


Fig. 7. Temperature-density diagram for gas particles in all dark (top row) and all bright (bottom row) galaxies. Each column corresponds to a different simulation, from left to right HESTIA 09_18, 17_11, 37_11, and NIVARIA-LG. The horizontal dashed line indicates the threshold temperature below which gas is able to form stars in NIVARIA-LG, whilst the vertical cyan and white lines show the corresponding density thresholds to set off SF in HESTIA ($n_{\text{th}} = 0.13 \text{ cm}^{-3}$) and NIVARIA-LG ($n_{\text{th}} = 10 \text{ cm}^{-3}$), respectively. The red continuous line in the T - ρ diagrams of *dark galaxies* correspond to the predicted temperature-density relation expected in RELHICs, as derived in Benítez-Llambay et al. (2017). Note that the *dark galaxy* histogram corresponding to HESTIA 37_11 is rather sparse, as only one object is found in that simulation.

NIVARIA-LG, respectively. Bright galaxies contain on average a significant amount of dense gas, while *dark galaxies* have little to no gas at densities larger than n_{th} .

In HESTIA simulations, bright galaxies display a region of dense gas in the upper-right part of the plots, owing to the implementation of an effective equation of state (EOS) that imposes an artificial pressure for gas above the star-formation density threshold (Grand et al. 2017, following the Springel & Hernquist 2003 model). This feature is instead absent in NIVARIA-LG, where the gas is treated as an ideal gas at all densities and a polytropic effective EOS for star-forming gas is not imposed (e.g. Stinson et al. 2012; Wang et al. 2015). In NIVARIA-LG, the more restrictive SF criterion ($n_{\text{th}} \geq 10 \text{ cm}^{-3}$) makes it more difficult for galaxies to convert their gas into stars: as a consequence, a given *dark galaxy* might be able to form some stars in HESTIA, but not in NIVARIA-LG. It shall be noted that the absence of gas particles above the SF density threshold in the T - ρ diagram for NIVARIA-LG bright galaxies, simply indicates that these systems are not currently forming stars at $z = 0$. However, they did experience SF at earlier epochs, in contrast to bright galaxies in HESTIA, which are predominantly star-forming at $z = 0$.

As demonstrated in Benítez-Llambay et al. (2017), gas within *dark galaxies* should exhibit a characteristic temperature-density relation arising from the combined effects of gas cooling at high densities and photoheating at low densities. This relation features a peak at $T \sim 4 \times 10^4 \text{ K}$ and $\rho \sim 10^{-4.8} \text{ cm}^{-3}$. This prediction, shown in the top, *dark galaxies* panels of Fig. 7 as a solid red line, is in very good agreement with results from our simulations. This relation reflects an approximate hydrostatic equilibrium between the gas and the halo gravitational potential, as well as thermal equilibrium with the UV background under the assumption of spherical symmetry. The gas properties of *dark galaxies* thus establish the conditions for little to no star formation and are consistent with the characteristics of their underlying DM haloes. Lower halo concentrations, lower halo masses at the epoch of reionization, and higher spin parameters compared to bright galaxies of similar mass, promote under-dense

gas to remain in hydrostatic and thermal equilibrium within its DM matter halo and to never form stars.

3.4. Spatial distribution and environment

In order to assess the impact of the intergalactic medium on the properties of *dark galaxies*, we analyse in this section whether dark and bright galaxies inhabit different environments and how the density of these surroundings evolves over time. Figure 8 shows the distribution of dark (magenta) and bright (green) galaxies in both the x - y and x - z projections for the four simulation runs at the present epoch. The figure displays a region centred on the MW analogue and extending to a radius of 2.5 Mpc. The background represents the superimposed DM and gas density fields. Bright galaxies are generally more concentrated in high-density regions, closer to the two main central haloes. In contrast, the distribution of *dark galaxies* appear to be more spatially extended, occupying larger radial distances and residing predominantly farther from the central regions and the bulk of the main filament. This trend is less evident in NIVARIA-LG, because the sample of bright galaxies is significantly smaller than that of *dark galaxies*; nevertheless, the trend is still present.

The larger distances from the MW at which *dark galaxies* are found are further illustrated in Fig. 9, which shows the cumulative distribution of the radial distances of all dark (magenta) and bright (green) galaxies from the MW analogues. The difference between the two radial distributions is again confirmed by a KS test, yielding a p -value of $\sim 10^{-10}$. This low value indicates that the two samples are statistically distinct. We find that 50% of the *dark galaxy* sample lies within 1.9 Mpc of the MW, whereas 50% of bright galaxies are located within 1.3 Mpc. Consequently, we expect a large fraction of *dark galaxies* to be found in the outskirts of the Local Group.

We take a step further and examine the evolution of the DM and gas densities within a spherical shell extending from $1R_{\text{vir}}$ to $7R_{\text{vir}}$ around each dark and bright galaxy identified at different redshifts. The results are shown in Fig. 10, where the median densities of all dark and bright galaxies from the four

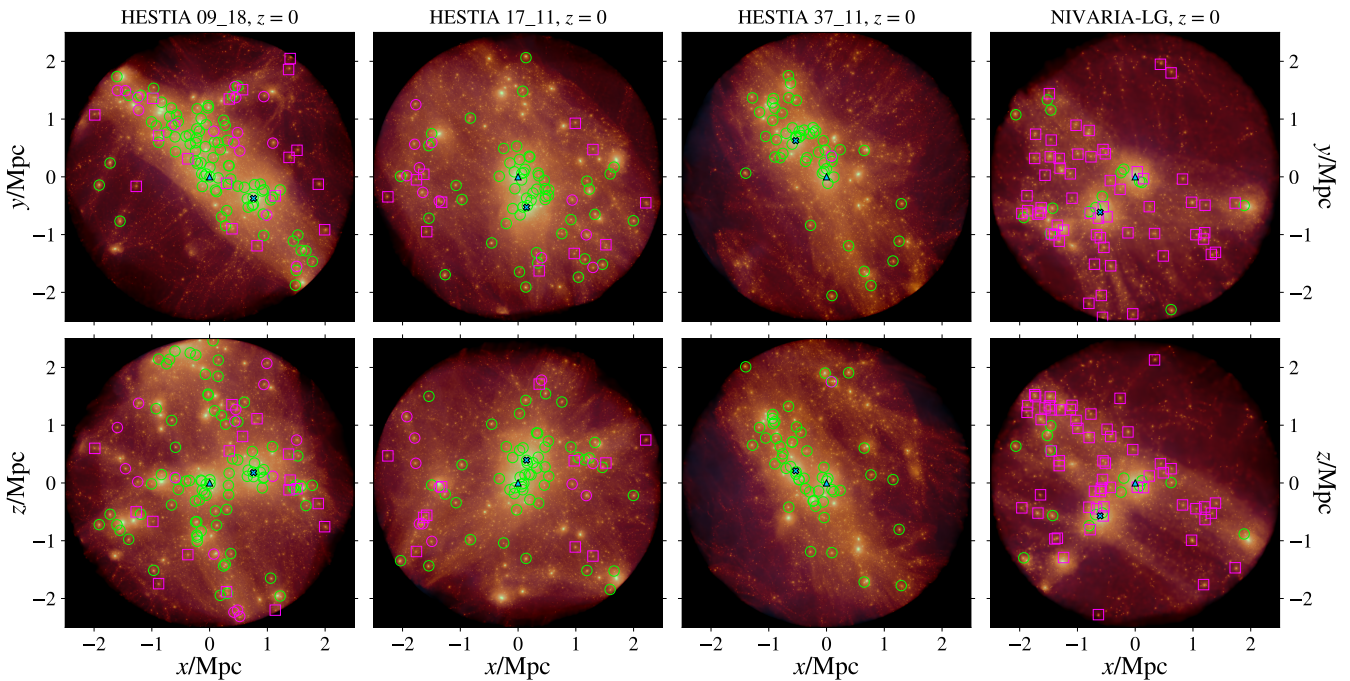


Fig. 8. Projected positions of dark (magenta) and bright (green) galaxies in x - y (top row) and x - z (bottom row) space at $z = 0$, within a sphere of 2.5 Mpc of radius from the MW. From the left to right, we present the three HESTIA simulations (09_18, 17_11, and 37_11) and NIVARIA-LG. Circles indicate *dark galaxies* with stars, whereas squares indicate the starless *dark galaxies*. The background shows the density of DM in orange and the gas density in yellow. The region is centred on the MW, shown as a blue triangle, while M31 is represented as a blue square.

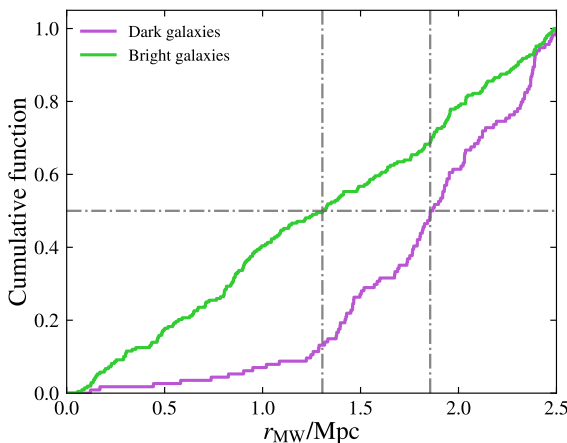


Fig. 9. Cumulative distribution of the radial distances of dark (magenta) and bright (green) galaxies with respect to the MW analogues for all four simulations at $z = 0$. The horizontal grey line marks the mean of the distributions, while the two vertical lines indicate the distances within which 50% of dark and bright galaxies are found, corresponding to $r_{\text{MW}} = 1.9$ Mpc and $r_{\text{MW}} = 1.3$ Mpc, respectively.

simulations are displayed in magenta and green, respectively. The shaded background regions represent the 16th and 84th percentiles of each distribution. Consistent with the results shown in Fig. 8, bright galaxies reside in environments with higher DM and gas densities than *dark galaxies*. These results indicate that *dark galaxies* originate in lower-density regions within the Local Group and remain in such environments throughout their lifetime. Their persistently lower DM and gas density environment make *dark galaxies* less susceptible to galaxy interactions, mergers, and gas inflows, allowing their gas to remain diffuse

and in equilibrium within their DM halo rather than collapsing. These results are in agreement with previous work from Benítez-Llambay et al. (2017), who showed that gas-rich RELHICs inhabit the under-dense outskirts of the APOSTLE simulations. In Appendix A, we present the same density evolution as shown in Fig. 10, but separately for each simulation.

3.5. $\text{H}\alpha$ detectability with FAST

Objects such as *dark galaxies*, which exhibit little to no luminous matter, are inherently difficult to identify observationally. Nevertheless, if they contain a substantial reservoir of $\text{H}\alpha$ they may be detectable as gas clouds via their 21 cm line emission, using facilities such as the FAST radio telescope. In this section, we present estimates of the detectability of *dark galaxies* based on their $\text{H}\alpha$ content, selecting FAST as the instrument of choice due to its large sky coverage and high sensitivity.

We estimate the amount of neutral atomic hydrogen in the HESTIA sample by adopting the empirical approach presented in Arjona-Gálvez et al. (2024). This method builds upon the phenomenological prescription introduced by Marinacci et al. (2017), itself based on Leroy et al. (2008). In this framework, the ratio between the molecular and atomic hydrogen column densities is fitted with a functional form that depends on the gas mid-plane pressure, which then allows us to infer the $\text{H}\alpha$ atomic fraction. On the other hand, the $\text{H}\alpha$ fraction in NIVARIA-LG is measured following the self-shielding approximation detailed in Rahmati et al. (2013), which uses the radiative transfer model from Pawlik & Schaye (2008, 2011).

Figure 11 shows the $\text{H}\alpha$ masses of the *dark galaxy* sample in HESTIA simulations (blue shades) and NIVARIA-LG (red), as a function of their DM halo masses. We include Cloud-9 as a

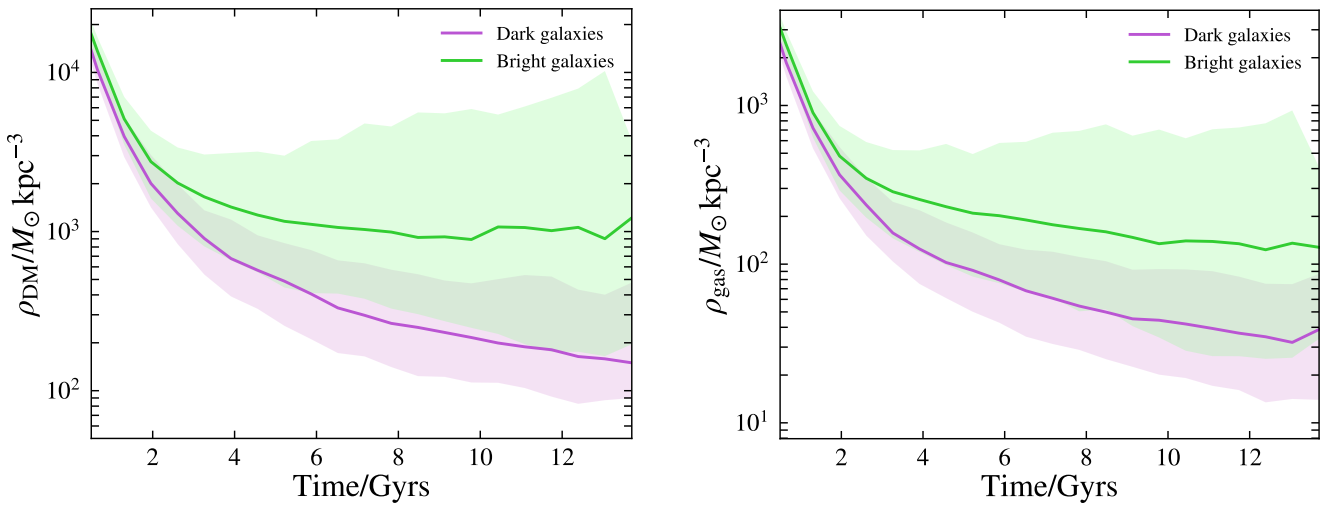


Fig. 10. Evolution of median DM (left panel) and gas (right panel) density of the environment around the full sample of *dark galaxies* in magenta and bright galaxies in green, combining all four simulations. The shaded backgrounds are the regions limited by the 16th and 84th percentiles of the distributions. The environment is defined as a spherical shell between $1 R_{\text{vir}}$ and $7 R_{\text{vir}}$ of each halo, at each redshift.

reference⁴. We can observe a very strong correlation between the halo mass and the H₁ gas in each *dark galaxy*. We perform an exercise to furnish a quick estimation on the detectability of these *dark galaxies* with FAST. Details on how the FAST limits are calculated can be found in Appendix B. The two shaded areas in Fig. 11 represent the region of detectability within 1 Mpc and 2.5 Mpc, according to the values obtained for the minimum H₁ mass detectable with FAST. Here, it can be seen that up to 18 of our *dark galaxies* fall in the region corresponding to distances within 1 Mpc, and up to 10 of those fall in the region within 2.5 Mpc. These maximum values are set by the NIVARIA-LG simulation, which contributes with the largest number of *dark galaxies* within the detectability region compared to the rest of simulations. It is also visible that several *dark galaxies* are below the detection limits for such distances.

In Fig. 12 we further clarify the distance dependence by showing H₁ masses of *dark galaxies* with respect to their distance from the simulated MW analogues. The grey dotted-dashed line represents the H₁ mass limit with respect to the distance, as given by Eq. B.3. All *dark galaxies* located above this line should be detectable by FAST in terms of their total H₁ mass and distance. The area of detectability is shown as the grey shaded region. In this case, the number of *dark galaxies* falling within said region is between 0 and 18, according to each one of the simulation runs used (where NIVARIA-LG provides the largest estimate, and HESTIA 37_11 the lowest).

We further explore the detectability of these galaxies by analysing their H₁ column density profiles, which are shown in Fig. 13, for HESTIA in the left panel and for NIVARIA-LG in the right panel. The profiles are coloured according to the H₁ mass of each *dark galaxy*, where darker colours indicate larger H₁ masses. The coloured vertical dotted-dashed lines indicate the softening length of each simulation, below which profiles are not well resolved. Since FAST can reach down to a median 3σ column density of $N_{\text{H}_1} = 2 \times 10^{17} \text{ cm}^{-2}$ (Pan et al. 2024), we show this limit in the panels as a grey horizontal dotted-dashed line. Hence, all galaxies whose profiles lie above this threshold

and within the grey shaded area would be detectable by FAST. We can see that all profiles with values exceeding the FAST column density detection limit (and beyond the softening length) have H₁ masses $> 10^4 M_{\odot}$. These results are added to Fig. 11 and Fig. 12, where we now indicate the halos corresponding to these minimum detectable column densities using concentric circles. Therefore, there is a trend for which the most massive *dark galaxies* in DM are generally those that can be detectable, in agreement with results from Benítez-Llambay et al. (2017). On the other hand, since the simulated *dark galaxies* have been centred and set in a face-on orientation, the N_{H_1} values shown in Fig. 13 are actually a lower limit, and could be slightly larger when placing the halos edge-on.

That said, the total number of *dark galaxies* with both sufficient H₁ mass and column densities to be detectable by FAST is up to 14 when using the NIVARIA-LG simulation, which therefore provides an upper limit: these galaxies are indicated as red symbols with concentric circles within the shaded grey region in Fig. 12. Conversely, only 5 and 7 *dark galaxies* would be detectable by FAST, if one trusts the HESTIA simulations (seeds 09_18 and 17_11). Since the simulations consider the whole sky, these values are effectively smaller when we account for the fact that FAST is located in the northern hemisphere and covers only $\sim 58\%$ of the total sky (e.g., Qian et al. 2020).

Consequently, the upper limit on the number of *dark galaxies* detectable within 2.5 Mpc from the MW, taking into account the FAST sky coverage and minimum H₁ mass and column density, is 8. This is our preferred value, based on the more realistic NIVARIA-LG simulations which, notably, produce all starless *dark galaxies*.

4. Discussion

We find that bright galaxies in our sample include a substantially higher fraction of satellites than *dark galaxies*, indicating that luminous systems are more frequently bound to larger hosts, while *dark galaxies* preferentially reside in isolation. This environmental distinction also appears in the satellite statistics of Lee et al. (2024), where star-rich galaxies exhibit higher satellite fractions than star-poor or starless systems. In our simula-

⁴ Note here Cloud-9 is not within the range of distances of our analysis, i.e. $d_{\text{Cloud-9}} \sim 4.7 \text{ Mpc}$.

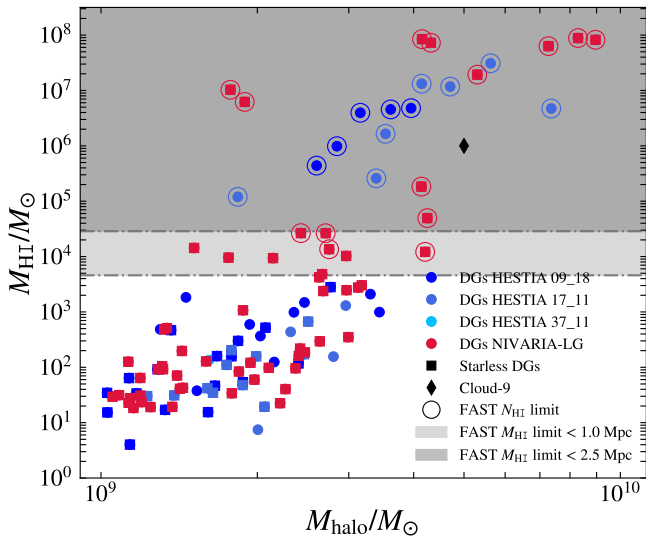


Fig. 11. Mass of H₁ versus DM halo mass for *dark galaxies* in each simulation, with HESTIA indicated as blue shades while NIVARIA-LG in red. Squares symbols denote starless *dark galaxies*. The grey shaded regions represent halos with H₁ masses that could be detectable with FAST in 1 hour integration time and at distances of < 1 Mpc and < 2.5 Mpc from the MW analogues. The concentric circles indicate *dark galaxies* whose central H₁ column densities exceed the FAST detection limit, N_{H_1} . We include Cloud-9 as a black diamond.

tions, these differences naturally place bright and *dark galaxies* in contrasting environments: bright galaxies experience more mergers, interactions, and tidal capture, whereas *dark galaxies* remain largely detached from dense environments and massive

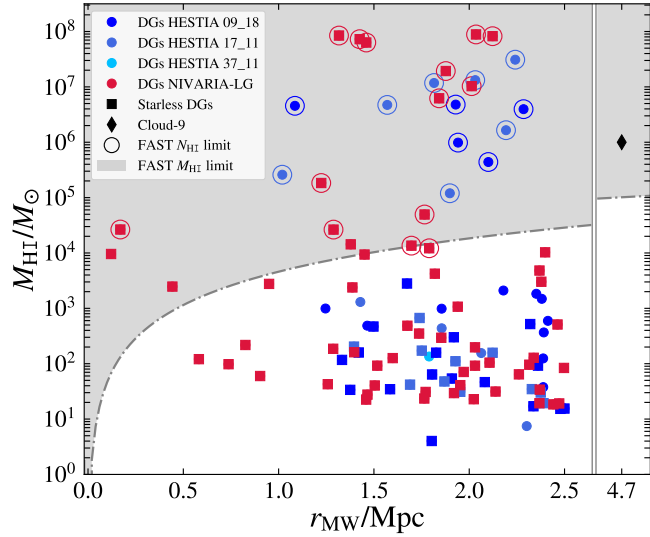


Fig. 12. H₁ mass versus radial distance of *dark galaxies* with respect to the MW analogues in each simulated run, with HESTIA indicated as blue symbols and NIVARIA-LG as red symbols. Squares correspond to starless *dark galaxies*. The grey dotted-dashed line represents the minimum H₁ mass that galaxies must have to be detectable by FAST, as a function of their distance from us. *Dark galaxies* likely to be detectable by FAST are those that fall within the shaded region. The concentric circles indicate *dark galaxies* whose central H₁ column densities N_{H_1} exceed the FAST detection limit. Cloud-9 is included as a black diamond at $d = 4.7$ Mpc.

hosts. This is fully consistent with the environmental-density trends presented in Sec. 3.4, which show that *dark galaxies* lie farther from the main filaments and central regions of the Local Group. Moreover, as shown in Fig. 10, not only do *dark galaxies* inhabit lower-density regions today, but they also originate in underdense environments, which can directly suppress SF by limiting gas accretion. This picture is also supported by observational results from Kwon et al. (2025), who find that potential *dark galaxy* candidates in the ALFALFA survey preferentially occupy low-density environments.

The distinct formation histories of bright and *dark galaxies* further reinforce this scenario. As shown in Fig. 4, *dark galaxies* assemble later ($z_{\text{dark}}=1.7\text{-}2.0$) than bright galaxies ($z_{\text{bright}}=2.6\text{-}3.2$), resulting in systematically lower concentrations (Fig. 5). Combined with their higher spin parameters, this implies that *dark galaxies* inhabit more extended, less concentrated halos that retain under-dense gas, below the SF threshold.

These findings are in excellent agreement with results from Benítez-Llambay et al. (2017) and Lee et al. (2024), even though their studies employed a different simulation suite, numerical methods, resolution and initial conditions. An important difference with the work of Lee et al. (2024), however, is that they do not require their sample of *dark galaxies* to necessarily contain H₁ gas, while in our selection we explicitly require H₁ gas to be present, so as to assess the detectability of *dark galaxies* with observational surveys. The comparison with Lee et al. (2024) should therefore be considered qualitative, since the *dark galaxy* samples in our work and theirs are selected using different underlying criteria.

5. Conclusions

In this work, we analysed the three high-resolution HESTIA simulation runs (Libeskind et al. 2020) and the new NIVARIA-LG simulation (Contreras-Santos et al. in prep.) to derive the properties of H₁-rich *dark galaxies* within Local Group-like volumes simulated with the same constrained initial conditions but with different numerical codes and galaxy-formation models (AREPO for the HESTIA simulation, GASOLINE2 for NIVARIA-LG). Across the four runs, we identified a total of 114 *dark galaxies* in the dark matter halo mass range $10^9\text{-}10^{10} M_{\odot}$, of which only six are satellites of larger galactic systems at $z = 0$. We then compared their properties to those of a control sample of bright galaxies within the same halo mass range. Our main conclusions are summarized below.

Dark galaxies:

- exist in Local Group simulations run with different codes and feedback models, with their abundance depending on the mass of the Local Group itself and, critically, on the adopted star formation density threshold n_{th} . Simulations that employ a more realistic, higher n_{th} , produce significantly more *dark galaxies* than those that do not (up to ~ 60 in the NIVARIA-LG run, compared to 17, 11 and 0 starless *dark galaxies* arising in the three HESTIA runs, respectively, as in Table 1);
- contain a similar total amount of gas as their bright-galaxy counterparts, although only the most massive *dark galaxies*, with $M_{\text{halo}} > 10^{9.5} M_{\odot}$, have large H₁ gas reservoirs comparable to those found in bright galaxies, i.e. $M_{\text{H}_1} > 10^5 M_{\odot}$ (Fig. 3). Such gas cannot form stars efficiently because of its low density, being in hydrostatic equilibrium within the gravitational potential of its halo (Fig. 7);

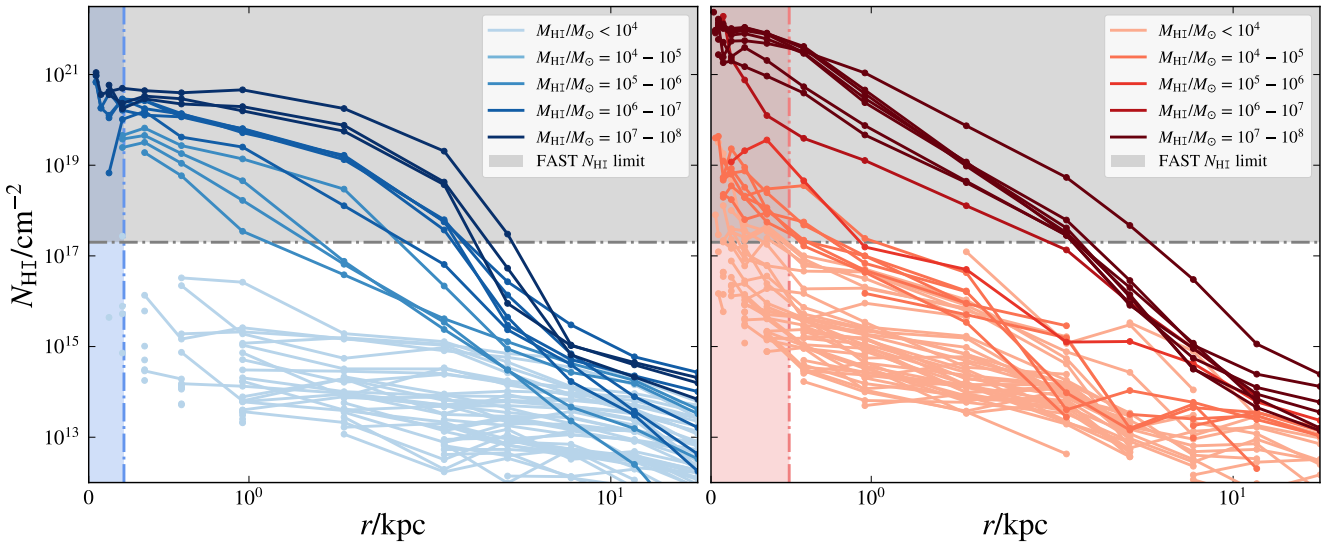


Fig. 13. $\mathrm{H}\alpha$ column density profiles of *dark galaxies* for the HESTIA simulations (left) and the NIVARIA-LG simulations (right), coloured by $\mathrm{H}\alpha$ mass. The grey dotted-dashed line represents the minimum $\mathrm{H}\alpha$ column density value that FAST can reach, which is $N_{\mathrm{H}\alpha} = 2 \times 10^{17} \mathrm{cm}^{-2}$. The coloured shaded area in each panel shows the softening length corresponding to each simulation. A smaller number of *dark galaxies* could be detected by the less sensitive ALFALFA Survey, $N_{\mathrm{H}\alpha} \gtrsim 10^{18} \mathrm{cm}^{-2}$.

- have lower masses than bright galaxies at the epoch of reionization, and throughout cosmic time (Fig. 4), which render them dark, since galaxy formation can occur only in haloes whose masses exceed a critical threshold (Benítez-Llambay & Frenk 2020);
- have $z = 0$ halo masses peaking at $\sim 2 \times 10^9 M_\odot$ (Fig. 2), higher spin parameters (Fig. 6) and lower concentrations (Fig. 5) than bright galaxies, consistent with their late formation times (Fig. 4);
- are located farther from the Milky Way than luminous galaxies (Fig. 9), with about 80% residing at distances greater than 1.5 Mpc, and they inhabit lower-density regions of the Local Group (Fig. 8);
- they formed and evolved across redshift within regions characterized by persistently lower dark matter and gas densities compared to the environments of bright galaxies, making them less susceptible to galaxy interactions, mergers, and gas inflows (Fig. 10);
- can be detected via their $\mathrm{H}\alpha$ emission. Using the sky coverage of the new FAST radio telescope, along with its minimum detectable $\mathrm{H}\alpha$ mass and column-density sensitivity, we predict that up to 8 *dark galaxies* should be detectable in $\mathrm{H}\alpha$ within 2.5 Mpc of the Local Group (Fig. 11 and Fig. 12).

The NIVARIA-LG simulation adopts a star formation density threshold, $n_{\mathrm{th}} = 10 \mathrm{cm}^{-3}$, that is more realistic than the HESTIA one, reflecting the densities of clumps within typical giant molecular clouds ($10\text{--}100 \mathrm{cm}^{-3}$). It produces a great match of the M_\star – M_{halo} relation over several orders of magnitude in halo mass (Fig. 1) and is the only simulation able to generate completely starless *dark galaxies* with substantial $\mathrm{H}\alpha$ masses, $M_{\mathrm{H}\alpha} > 10^{4\text{--}5} M_\odot$ (Fig. 11 and Fig. 12). Thanks to its physically motivated star-formation recipe, NIVARIA-LG is likely to provide the most reliable predictions for *dark galaxies* with sufficient $\mathrm{H}\alpha$ to be detectable. Indeed, while all *dark galaxies* remain completely starless in NIVARIA-LG, the low star-formation density threshold adopted in HESTIA allows some *dark galaxies* to form a small number of stars.

The study of *dark galaxies* is currently a highly active field of research, driven by the increasing availability of both observational data and theoretical predictions. Improvements in observational techniques are expanding the number of *dark galaxies* candidates, while advances in numerical simulations, now able to reproduce many of the key processes governing galaxy formation and evolution, are proving essential for interpreting these systems. Together, these developments are pushing the field forward and bringing us closer to a robust confirmation of genuine *dark galaxies*. Such objects would serve as powerful cosmological probes of the Λ CDM model, and their detection would provide strong support for it. We expect upcoming observations with FAST, along with other radio telescopes, to aid in the detection of $\mathrm{H}\alpha$ sources harboured within a dark matter halo. Future work should focus on measuring the gas metallicity within *dark galaxies*, to determine whether truly starless systems indeed contain primordial, metal-free gas, and to assess whether any past star-formation episodes may have occurred.

Acknowledgements. We thank Julio Navarro, Duncan Forbes, Jonah Gannon and Marco Monaci for useful discussions. A. Di Cintio, G. García-Bethencourt and A. Contreras-Santos acknowledge financial support from the Spanish Ministry of Science and Innovation (MICINN) from the EU Next Generation Funds under the 2023 Consolidación Investigadora program, CNS2023-144669, project "Tiny" (PI A. Di Cintio). SC acknowledges funding from the State Research Agency (AEI-MICIU) of the Spanish Ministry of Science, Innovation, and Universities under the grant with reference PID2023-149139NB-I00. E. Arjona-Gálvez acknowledges support from the Agencia Espacial de Investigación del Ministerio de Ciencia e Innovación (AEI-MICIN) and the European Social Fund (ESF+) through a FPI grant PRE2020-096361. SCB acknowledges financial support from the Spanish Ministry of Science and Innovation (MICINN) through RYC2022-035838-I, PID2021-128131NB-I00 (CoBEARD) and CNS2022-135482 projects. AN is supported by the applied research and innovation project (SOL2024-31834, PI Andrea Negri), co-financed by the EU - Ministry of Finance and Public Service - European Funds - Junta de Andalucía - Consejería de Universidad, Investigación e Innovación. AK is supported by project PID2024-156100NB-C21 financed by MICIU /AEI/10.13039/501100011033 / FEDER, UE and further thanks Fontaines DC for hurricane laughter. The NIVARIA-LG simulations have been run using *LaPalma* supercomputer, project *can43* (PI A. Di Cintio). The author(s) wish to acknowledge the contribution of the IAC High-Performance Computing support team.

References

Arjona-Gálvez, E., Cardona-Barrero, S., Grand, R. J. J., et al. 2025, A&A, 699, A301

Arjona-Gálvez, E., Di Cintio, A., & Grand, R. J. J. 2024, A&A, 690, A286

Arora, N., Macciò, A. V., Courteau, S., et al. 2022, MNRAS, 512, 6134

Benítez-Llambay, A. & Frenk, C. 2020, Monthly Notices of the Royal Astronomical Society, 498, 4887

Benítez-Llambay, A. & Navarro, J. F. 2023, ApJ, 956, 1

Benítez-Llambay, A., Navarro, J. F., Abadi, M. G., et al. 2013, ApJ, 763, L41

Benítez-Llambay, A., Navarro, J. F., Frenk, C. S., et al. 2017, MNRAS, 465, 3913

Benítez-Llambay, A., Dutta, R., Fumagalli, M., & Navarro, J. F. 2024, The Astrophysical Journal, 973, 61

Blank, M., Macciò, A. V., Dutton, A. A., & Obreja, A. 2019, MNRAS, 487, 5476

Brook, C. B., Di Cintio, A., Knebe, A., et al. 2014, ApJ, 784, L14

Brook, C. B., Stinson, G., Gibson, B. K., Wadsley, J., & Quinn, T. 2012, MNRAS, 424, 1275

Bullock, J. S., Dekel, A., Kolatt, T. S., et al. 2001, ApJ, 555, 240

Carlesi, E., Sorce, J. G., Hoffman, Y., et al. 2016, MNRAS, 458, 900

Chabrier, G. 2003, PASP, 115, 763

Contreras-Santos, A. et al. in prep.

Duffy, A. R., Battye, R. A., Davies, R. D., Moss, A., & Wilkinson, P. N. 2008, MNRAS, 383, 150

Dutton, A. A. & Macciò, A. V. 2014, MNRAS, 441, 3359

Dutton, A. A., Obreja, A., Wang, L., et al. 2017, MNRAS, 467, 4937

Fattahi, A., Navarro, J. F., Sawala, T., et al. 2016, Monthly Notices of the Royal Astronomical Society, 457, 844

Ferland, G. J., Korista, K. T., Verner, D. A., et al. 1998, PASP, 110, 761

Gill, S. P. D., Knebe, A., & Gibson, B. K. 2004, MNRAS, 351, 399

Giovanelli, R., Haynes, M. P., Kent, B. R., et al. 2005, AJ, 130, 2598

Girelli, G., Pozzetti, L., Bolzonella, M., et al. 2020, A&A, 634, A135

Gottlöber, S., Hoffman, Y., & Yepes, G. 2010, arXiv e-prints, arXiv:1005.2687

Grand, R. J. J., Gómez, F. A., Marinacci, F., et al. 2017, MNRAS, 467, 179

Gunn, J. E. & Gott, III, J. R. 1972, ApJ, 176, 1

Haardt, F. & Madau, P. 1996, ApJ, 461, 20

Haynes, M. P., Giovanelli, R., Kent, B. R., et al. 2018, ApJ, 861, 49

Haynes, M. P., Giovanelli, R., Martin, A. M., et al. 2011, AJ, 142, 170

Hoeft, M., Yepes, G., Gottlöber, S., & Springel, V. 2006, MNRAS, 371, 401

Hoffman, Y. & Ribak, E. 1991, ApJ, 380, L5

Ikeuchi, S. 1986, Ap&SS, 118, 509

Jimenez, R. & Heavens, A. F. 2020, Monthly Notices of the Royal Astronomical Society: Letters, 498, L93

Kennicutt, Jr., R. C. 1998, ApJ, 498, 541

Kent, B. R., Giovanelli, R., Haynes, M. P., et al. 2007, ApJ, 665, L15

Knollmann, S. R. & Knebe, A. 2009, ApJS, 182, 608

Kwon, M., Hwang, H. S., Kent, B. R., et al. 2025, ApJS, 279, 38

Lee, G., Hwang, H. S., Lee, J., Shin, J., & Song, H. 2024, ApJ, 962, 129

Leroy, A. K., Walter, F., Brinks, E., et al. 2008, AJ, 136, 2782

Li, D., Stringer, A., Brown, P. E., Eadie, G. M., & Abraham, R. G. 2025a, The Annals of Applied Statistics, 19, 261

Li, D. D., Liu, Q., Eadie, G. M., et al. 2025b, The Astrophysical Journal Letters, 986, L18

Li, J., Wang, Y.-G., Kong, M.-Z., et al. 2018, Research in Astronomy and Astrophysics, 18, 003

Libeskind, N. I., Carlesi, E., Grand, R. J. J., et al. 2020, MNRAS, 498, 2968

Libeskind, N. I., Yepes, G., Knebe, A., et al. 2010, MNRAS, 401, 1889

Macciò, A. V., Udrescu, S. M., Dutton, A. A., et al. 2016, MNRAS, 463, L69

Marinacci, F., Grand, R. J. J., Pakmor, R., et al. 2017, MNRAS, 466, 3859

Martínez-Delgado, D., Roca-Fàbrega, S., Miró-Carretero, J., et al. 2023, A&A, 669, A103

Meyer, M., Robotham, A., Obreschkow, D., et al. 2017, PASA, 34, 52

Moster, B. P., Naab, T., & White, S. D. M. 2013, MNRAS, 428, 3121

Navarro, J. F., Frenk, C. S., & White, S. D. M. 1996, ApJ, 462, 563

Navarro, J. F., Frenk, C. S., & White, S. D. M. 1997, ApJ, 490, 493

Nebrin, O., Giri, S. K., & Mellema, G. 2023, Monthly Notices of the Royal Astronomical Society, 524, 2290

Nelson, D., Pillepich, A., Springel, V., et al. 2019, MNRAS, 490, 3234

Okamoto, T., Gao, L., & Theuns, T. 2008, MNRAS, 390, 920

Pakmor, R., Springel, V., Bauer, A., et al. 2016, MNRAS, 455, 1134

Pan, H., Jarvis, M. J., Zhu, M., et al. 2024, MNRAS, 534, 202

Pawlak, A. H. & Schaye, J. 2008, MNRAS, 389, 651

Pawlak, A. H. & Schaye, J. 2011, MNRAS, 412, 1943

Pereira-Wilson, M., Navarro, J. F., Benítez-Llambay, A., & Santos-Santos, I. 2023, MNRAS, 519, 1425

Pillepich, A., Nelson, D., Springel, V., et al. 2019, MNRAS, 490, 3196

Planck Collaboration, Ade, P. A. R., Aghanim, N., et al. 2014, A&A, 571, A16

Pontzen, A., Roškar, R., Stinson, G., & Woods, R. 2013, Astrophysics Source Code Library, record ascl:1305.002

Qian, L., Yao, R., Sun, J., et al. 2020, The Innovation, 1, 100053

Rahmati, A., Pawlik, A. H., Raičević, M., & Schaye, J. 2013, MNRAS, 430, 2427

Rees, M. J. 1986, MNRAS, 218, 25P

Roberts, M. S. 1975, in Galaxies and the Universe, ed. A. Sandage, M. Sandage, & J. Kristian, 309

Santos-Santos, I. M., Di Cintio, A., Brook, C. B., et al. 2018, MNRAS, 473, 4392

Sawala, T., Frenk, C. S., Fattahi, A., et al. 2016, Monthly Notices of the Royal Astronomical Society, 457, 1931

Schmidt, M. 1959, ApJ, 129, 243

Shen, S., Wadsley, J., & Stinson, G. 2010, MNRAS, 407, 1581

Sorce, J. G., Gottlöber, S., Yepes, G., et al. 2016, MNRAS, 455, 2078

Springel, V. 2010, MNRAS, 401, 791

Springel, V. & Hernquist, L. 2003, MNRAS, 339, 289

Stinson, G. S., Brook, C., Macciò, A. V., et al. 2012, MNRAS, 428, 129

Trentham, N., Möller, O., & Ramirez-Ruiz, E. 2001, MNRAS, 322, 658

Tully, R. B., Courtois, H. M., Dolphin, A. E., et al. 2013, AJ, 146, 86

Vogelsberger, M., Genel, S., Sijacki, D., et al. 2013, MNRAS, 436, 3031

Wadsley, J. W., Keller, B. W., & Quinn, T. R. 2017, MNRAS, 471, 2357

Wang, L., Dutton, A. A., Stinson, G. S., et al. 2015, MNRAS, 454, 83

Weinberger, R., Springel, V., & Pakmor, R. 2020, ApJS, 248, 32

White, S. D. M. & Rees, M. J. 1978, MNRAS, 183, 341

Zaroubi, S., Hoffman, Y., & Dekel, A. 1999, ApJ, 520, 413

Zhang, C.-P., Zhu, M., Jiang, P., et al. 2024, Science China Physics, Mechanics, and Astronomy, 67, 219511

Zhou, R., Zhu, M., Yang, Y., et al. 2023, The Astrophysical Journal, 952, 130

Appendix A: Evolution of the density of the environment

We present in Fig. A.1 the median densities of the environment around dark and bright galaxies for each simulation individually. In this figure, *dark galaxies* are represented as dotted-dashed lines and bright galaxies as solid lines. Here, the peaks are owing to pericentric passages of halos that become satellites of other galaxies at different times, and therefore the density of their environment rises steeply because of the presence of a larger galaxy. Note that the cyan dotted-dashed line refers to the only *dark galaxy* found in the HESTIA run 37_11, which is currently a satellite galaxy (see Table 1).

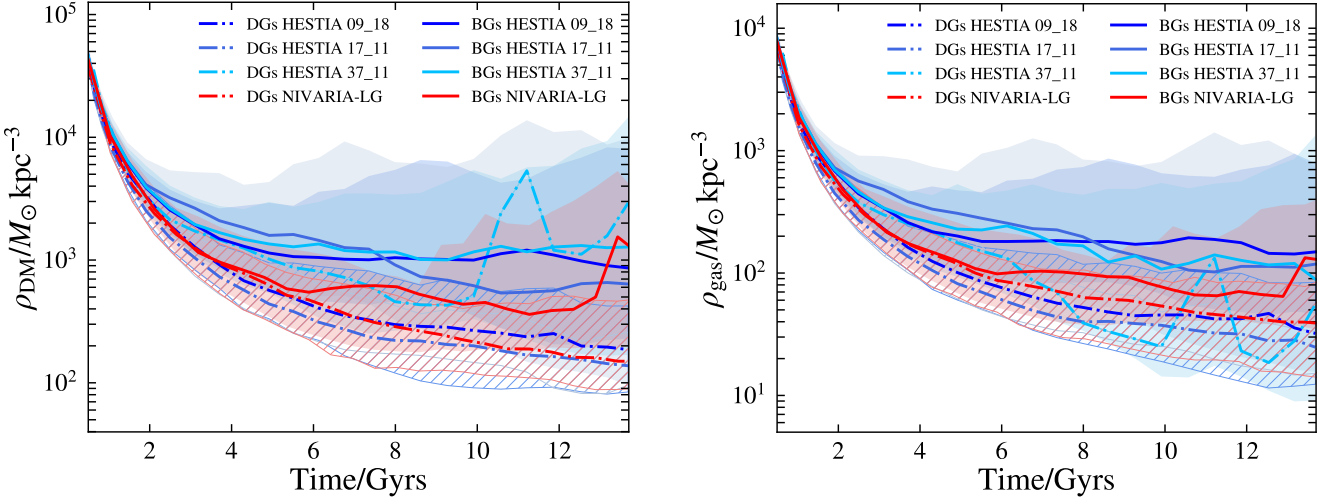


Fig. A.1. Evolution of median DM (*left panel*) and gas (*right panel*) density of the environment around dark and bright galaxies. *Dark galaxies* are shown as dotted-dashed lines and bright galaxies as solid lines. Each colour represents a different simulation, blue shades for HESTIA and red for NIVARIA-LG. The shaded and striped backgrounds are the regions limited by the 16th and 84th percentiles of the distributions. The environment is defined as a spherical shell between one R_{vir} and 7 R_{vir} of each halo at each time.

Appendix B: FAST detection limits

We follow the procedure presented in [Li et al. \(2018\)](#), done to obtain the integration time and number of detectable galaxies.

Firstly, we need the thermal noise associated to the instrument ([Duffy et al. 2008](#)):

$$\sigma_{\text{noise}} = \sqrt{2} \frac{kT_{\text{sys}}}{A_{\text{eff}}} \frac{1}{\sqrt{\Delta\nu t}} \quad (\text{B.1})$$

where $k = 1380 \text{ Jy m}^2 \text{ K}^{-1}$ is the Boltzmann constant, T_{sys} is the temperature of the system, A_{eff} is the aperture efficiency of the telescope, $\Delta\nu$ is the frequency bandwidth, and t is the integration time.

Once the thermal noise is obtained, we can compute the minimum observed flux limit at which a galaxy can be detected at $z = 0$. This threshold is given by the following expression ([Duffy et al. 2008](#)):

$$S_{\text{lim}} = (\text{S/N}) \sigma_{\text{noise}} \quad (\text{B.2})$$

where S/N is the signal-to-noise ratio.

Now, the minimum $\text{H}\alpha$ mass that a galaxy needs to have in order to be detectable by FAST at $z = 0$ can be directly derived as follows (e.g. [Roberts 1975](#); [Meyer et al. 2017](#)):

$$\frac{M_{\text{H}\alpha}}{M_{\odot}} = 2.35 \times 10^5 \left(\frac{d}{\text{Mpc}} \right)^2 \left(\frac{S_{\text{lim}}}{\text{Jy}} \right) \left(\frac{\Delta V_0}{\text{km s}^{-1}} \right) \quad (\text{B.3})$$

where d is the luminosity distance, and ΔV_0 is the velocity linewidth.

We adopt the same parameters as in [Li et al. \(2018\)](#). This is an aperture efficiency of $A_{\text{eff}} = 5 \times 10^4 \text{ m}^2$ for the spherical main reflector of FAST; a system temperature of $T_{\text{sys}} = 25 \text{ K}$, correspondent to the 21 cm line at 1.4 GHz within the L -band; a frequency bandwidth of $\Delta\nu = 10^6 \text{ Hz}$; a velocity linewidth of $\Delta V_0 = 200 \text{ km s}^{-1}$; and a signal-to-noise ratio of $\text{S/N} = 6$. Lastly, we set $z = 0$, assume 1 hour of observing time, and obtain $M_{\text{H}\alpha}$ for two different distances, namely $\sim 1 \text{ Mpc}$ and $\sim 2.5 \text{ Mpc}$. This setup results in minimum masses of $M_{\text{H}\alpha}(1 \text{ Mpc}) = 4.6 \times 10^3 M_{\odot}$, and $M_{\text{H}\alpha}(2.5 \text{ Mpc}) = 2.9 \times 10^4 M_{\odot}$ for galaxies within 1 Mpc and 2.5 Mpc⁵, respectively.

⁵ Note that d in Eq. B.3 refers to luminosity distance from earth, whilst our distances are measured with respect to the AHF centre of the MW analogues.